

Effect of gold composition on the orientations of oxide nuclei during the early stage oxidation of Cu-Au alloys

Langli Luo, Yihong Kang, Judith C. Yang, and Guangwen Zhou

Citation: *J. Appl. Phys.* **111**, 083533 (2012); doi: 10.1063/1.4707929

View online: <http://dx.doi.org/10.1063/1.4707929>

View Table of Contents: <http://jap.aip.org/resource/1/JAPIAU/v111/i8>

Published by the [American Institute of Physics](#).

Related Articles

Influence of boron doping on magnetic properties and microwave characteristics of MnIr/FeCoB multilayers
J. Appl. Phys. **111**, 083920 (2012)

Observation of dual magnonic and phononic bandgaps in bi-component nanostructured crystals
Appl. Phys. Lett. **100**, 163118 (2012)

A new pulsed laser deposition technique: Scanning multi-component pulsed laser deposition method
Rev. Sci. Instrum. **83**, 043901 (2012)

Smallest separation of nanorods from physical vapor deposition
Appl. Phys. Lett. **100**, 141605 (2012)

Exchange anisotropy in the nanostructured MnAl system
Appl. Phys. Lett. **100**, 112408 (2012)

Additional information on J. Appl. Phys.

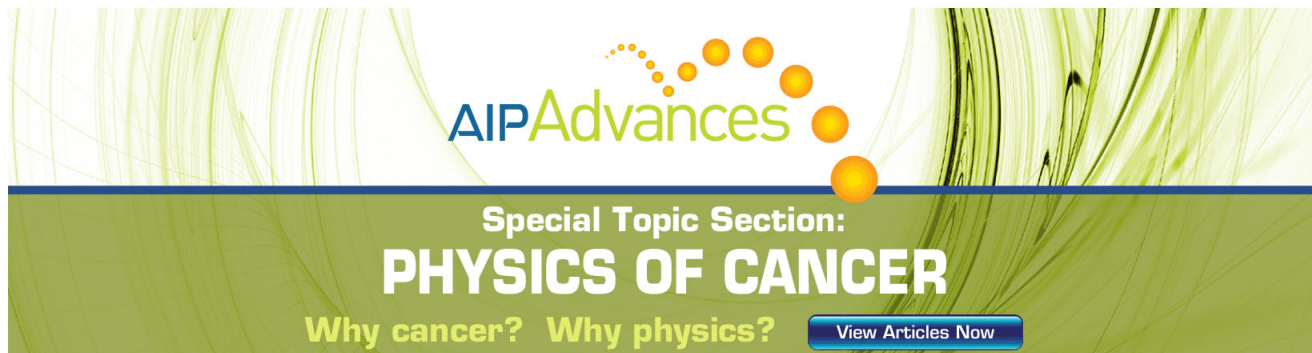
Journal Homepage: <http://jap.aip.org/>

Journal Information: http://jap.aip.org/about/about_the_journal

Top downloads: http://jap.aip.org/features/most_downloaded

Information for Authors: <http://jap.aip.org/authors>

ADVERTISEMENT



AIP Advances

Special Topic Section:
PHYSICS OF CANCER

Why cancer? Why physics? [View Articles Now](#)

Effect of gold composition on the orientations of oxide nuclei during the early stage oxidation of Cu-Au alloys

Langli Luo,¹ Yihong Kang,² Judith C. Yang,³ and Guangwen Zhou^{1,a)}

¹Department of Mechanical Engineering and Multidisciplinary Program in Materials Science and Engineering, State University of New York, Binghamton, New York 13902, USA

²Department of Mechanical Engineering and Materials Science, University of Pittsburgh, Pittsburgh, Pennsylvania 15261, USA

³Department of Chemical and Petroleum Engineering, University of Pittsburgh, Pittsburgh, Pennsylvania 15261, USA

(Received 19 January 2012; accepted 23 March 2012; published online 27 April 2012)

In situ environmental transmission electron microscopy is employed to study the effect of Au composition in Cu-Au alloys on the orientations of oxide islands during the initial-stage oxidation of Cu-Au(100) alloys. An orientation transition from nucleating epitaxial Cu₂O islands to randomly oriented oxide islands is observed upon increasing the oxygen gas pressure. By increasing the Au composition in the Cu-Au alloys, both the oxide nucleation time and saturation density of oxide islands increase, but the critical oxygen pressure leading to nucleating randomly oriented Cu₂O islands decreases. It is shown by a kinetic model that such a dependence of the critical oxygen pressure on the alloy composition is related to its effect on two competing processes, the oxide-alloy structure match and the effective collision of oxygen atoms, in determining the overall nucleation rate of oxide islands during the oxidation. © 2012 American Institute of Physics.

[<http://dx.doi.org/10.1063/1.4707929>]

I. INTRODUCTION

Fundamental understanding of the early stages of oxidation of metals and alloys is of great importance for many technologically important processes including corrosion, catalysis, microelectronic packaging, and synthesis of self-assembled nanostructures of metal oxide. For instance, Cu and Au alloy are widely used as conducting and packaging materials for tracks on printed wiring board (PWB), lead frames, interconnection wires, foils for flexible circuits, and heat sinks in microelectronic packaging. The environmental stability of Cu and Au alloys and their resistance to oxidation are highly desired for these applications,¹⁻³ and it becomes a more crucial problem when the dimensions of fabricated semiconductor devices shrink to the nanoscale. The interest in fundamental understanding of early stage oxidation of metals is not only because of its relevance to controlling metal oxidation but is also motivated by the numerous applications where surface oxides play a critical role. Metal and metal oxides are widely used as heterogeneous catalysts in industry, and their catalytic properties are intimately related to the oxidation states of metal atoms and surface morphology of the oxide film formed on metal surfaces. It has been increasingly apparent that the catalytic active phase for some transitional metals is in fact their oxides rather than the pure metals.^{4,5}

Generally, the oxidation of metals and alloys involves hierarchical multiple length scales and proceeds from oxygen surface chemisorption to oxide nucleation and growth and then to the formation of a continuous, macroscopically

thick oxide layer. Over the past decades, surface science studies on the oxidation of metal surfaces under idealized conditions, i.e., ultrahigh vacuum (UHV), have provided a wealth of knowledge on the microscopic processes of oxygen chemisorption including oxygen adsorption induced surface restructuring, adsorption sites, and reaction pathways.⁶ In the traditional studies of oxidation, much attention has been devoted to the kinetics of growing continuous oxide films by measuring the weight gain and oxygen consumption using thermogravimetric analysis (TGA), thereby identifying the dominant migrating species (i.e., cations, anions, or vacancies) controlling the oxidation rate.⁷ Therefore, a still poorly understood regime in metal oxidation is its transient early stages, i.e., oxide nucleation and growth at the nanoscale. Investigation of the nanoscale oxidation of metals and alloys is, therefore, highly desired for bridging the information gap between the knowledge obtained from the surface science methods which mainly focus on the oxygen adsorption of up to one monolayer and that of the traditional oxidation studies of bulk oxide growth.

A key challenge in understanding these early stages of the oxidation of metals and alloys has been the scarcity of structural information obtained *in situ* during oxidation, due, in large part, to the inability of traditional experimental techniques to perform *in situ* measurements of the structures and kinetics at the nanoscale as the reaction progresses. *In situ* environmental transmission electron microscopy (TEM) techniques solve this limitation by introducing reactive gases to specimens at the nanoscale and therefore significantly broaden the conditions of observation.^{8,9} The unique aspect of *in situ* TEM experiments is to provide dynamic information from nucleation to growth and coalescence of oxide islands at the nanometer scale under the controlled oxidation conditions,

^{a)}Author to whom correspondence should be addressed. Electronic mail: gzhou@binghamton.edu.

which is inaccessible by both surface science and traditional bulk oxidation methods but is essential for understanding the atomistic initial-stage oxidation kinetics. Using *in situ* TEM techniques, the oxidation of pure copper has been extensively investigated, and it has been shown that the early stage oxidation of copper typically involves nucleation and growth of oxide islands in which the oxygen surface diffusion plays a dominant role in determining the initial oxidation kinetics.^{10–14} These observations represent a departure from the classic theories of metal oxidation which assume uniform, layer-by-layer growth of continuous oxide films.^{15,16}

Compared to the extensive research on the oxidation of pure metals, the studies on the initial oxidation of alloys have been significantly fewer. This is largely due to the complexities associated with the oxidation of alloys, which include different oxygen affinities of the alloying elements, redistribution and segregation of the alloying elements, the formation of multiple oxide phases and the solid solubility between them, various mobilities of metal ions in the oxide phase, and different diffusivities of metals in the alloy. Choosing Cu-Au as model system, we studied the effect of alloying on the growth morphologies of oxide nanoislands, and a square-to-dendritic transition has been observed.¹⁷ In this work, we perform a detailed *in situ* TEM study of the early stage oxidation kinetics of Cu-Au alloys containing a noble metal and an oxidizable metal and seek the effects of alloying on nucleation orientations of oxide nanoislands. The Cu-Au system is selected since it allows for some of the features of alloy oxidation to be examined without the complication of the simultaneous formation of multiple oxides. Also, at temperatures $>400^\circ\text{C}$, where the oxidation behavior is of most interest, Cu and Au are fully miscible (the Cu-Au system is single phase face-centered cubic above 400°C for all composition and only one of the components oxidizes).

On the other hand, most of the studies of initial stages of metal and alloy oxidation have been performed under high vacuum conditions while technological applications such as catalytic reactions or oxidation-induced failures in micro-electronic devices occur typically under ambient or near atmospheric condition. Therefore, detailed study of the oxidation behavior under practical gas conditions is highly desired, and some recent studies revealed the reaction mechanisms can be indeed significantly different between UHV conditions and ambient gas pressures.^{5,18–28} In this work, we study the oxidation of Cu-Au(100) alloys under the realistic conditions of the oxygen gas pressure varying from 5×10^{-5} to 760 Torr by investigating the effect of alloying Cu with Au on the nucleation orientations of oxide islands. Our study reveals a transition from nucleating epitaxial Cu_2O nanoislands to non-epitaxial oxide islands upon increasing the oxygen gas pressure, and this pressure depends sensitively on the Au mole fraction in the Cu-Au alloys. By varying Au concentration from 5% to 50% (atomic percentage) in the Cu-Au(100) alloys, we observe that the critical oxygen pressure leading to nucleating randomly oriented oxide islands decreases with the increased Au composition for the same oxidation temperature. Our kinetic model reveals that this behavior is related to the dependence of the oxide nucleation barrier on the alloy compositions that modify the critical

oxygen gas pressure leading to the orientation transitions of oxide nuclei.

II. EXPERIMENTAL

Single crystal $\sim 700 \text{ \AA}$ thick Cu-Au(100) alloy thin films of different compositions were epitaxially grown on NaCl(100) substrates in an electron-beam evaporator by co-deposition at 400°C . The thickness of 700 \AA of free standing Cu-Au films was chosen so that the alloy films were thin enough to be examined by the TEM but thick enough for the oxidation behavior as close as to that of bulk metal. The composition of the thin film was controlled by adjusting the evaporation rates of the Cu and Au sources. The alloy thin films were removed from NaCl substrates by floating in deionized water, washed and mounted on a specially designed TEM holder that allows for resistive heating up to $\sim 1000^\circ\text{C}$. The film compositions were calibrated by TEM x-ray energy dispersive spectroscopy (EDS) analysis, and the single-crystallinity and orientations of the alloy films were checked by TEM electron diffraction. Our *in situ* oxidation experiments were carried out in a modified JEOL 200CX TEM. This microscope is equipped with an UHV chamber with a base pressure at $\sim 10^{-8}$ Torr. A leak valve attached to the column permits introduction of gases directly into the TEM with a controlled oxygen gas pressure ($p\text{O}_2$) ranging from 5×10^{-5} Torr to 760 Torr, which can be monitored by a full range vacuum gauge. Before the oxidation experiments, any native oxide was removed by annealing in the TEM chamber at 750°C under vacuum condition^{29,30} or *in situ* annealing under H_2 gas at pressure $\sim 10^{-5}$ Torr and 350°C , resulting in a clean surface. The sample cleanliness was checked by EDS analysis and electron diffraction. Oxygen gas of 99.999% purity was then admitted into the column of the microscope through the leak valve to oxidize cleaned alloy films at 400°C under a constant $p\text{O}_2$ between 5×10^{-5} Torr and 760 Torr. Real time TEM observations of the oxidation can be made at pressures $\leq 8 \times 10^{-4}$ Torr. For the higher $p\text{O}_2$, the electron gun is isolated from the TEM column during the oxidation, and TEM characterization was made immediately after the oxidation by quickly pumping the TEM column to vacuum. TEM techniques including electron diffraction, bright and dark field imaging, high-resolution TEM, and electron moiré fringe imaging were utilized to determine the orientation relationships of oxide islands with the Cu-Au alloy substrate.

III. EXPERIMENTAL RESULTS

After introducing oxygen gas to the TEM chamber, no oxide islands emerge on the Cu-Au surface immediately. After an incubation time, visible embryos ($\sim 10 \text{ nm}$) of Cu_2O islands can be observed, and the number density of oxide islands increases and reaches a saturation density with the continued oxidation. It is observed that the saturation time (the time required for reaching the saturated density of oxide islands) depends on both the oxygen partial pressure and Au concentration in the Cu-Au alloys. The higher oxygen pressure results in a faster oxide nucleation rate and therefore a shorter saturation time for samples with the same Au

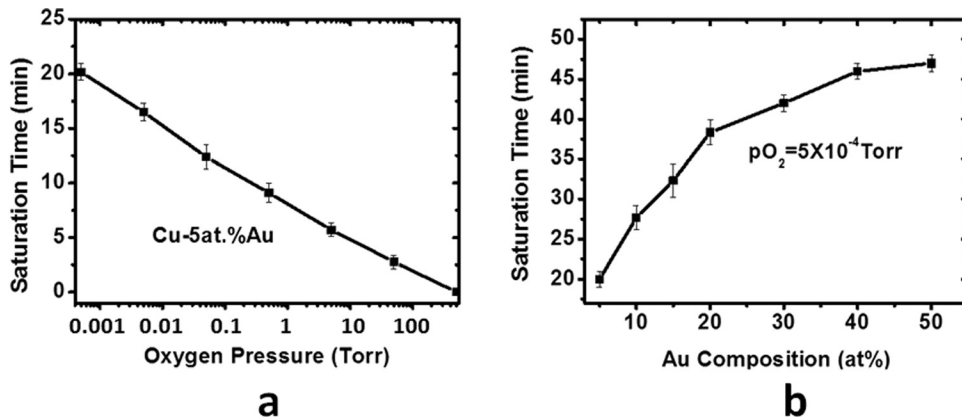


FIG. 1. (a) Dependence of the saturation time for reaching the saturated density of oxide islands on the oxygen partial pressure for the oxidation of Cu-5 at. % Au(100) at 400 °C and (b) dependence of the saturation time of oxide nucleation on the Au composition during the oxidation of Cu-Au(100) alloys at 400 °C and $p_{O_2} = 5 \times 10^{-4}$ Torr.

composition, while for the same oxygen pressure, increasing the Au content in the alloy leads to a longer saturation time. As shown in Fig. 1, for instance, the saturation time is ~ 15 min for the oxidation of a Cu-5 at. % Au(100) alloy at $p_{O_2} = 5 \times 10^{-3}$ Torr and $T = 400$ °C while it is ~ 5 min for the oxidation at $p_{O_2} = 5$ Torr and $T = 400$ °C. Fig. 1(b) shows the dependence of the saturation time on the Au composition, i.e., for the same oxygen gas pressure and oxidation temperature, a larger Au composition leads to a slower nucleation rate of oxide islands and thus a longer saturation time.

In situ TEM imaging is also used to determine the number density of oxide islands during the oxidation of Cu-Au alloys. The measurements indicate that the saturation density of oxide islands depends on both the oxygen gas pressure and Au composition. Fig. 2 shows the dependence of the saturation density of oxide islands as a function of the Au composition varying from 5 at. % to 50 at. % in the Cu-Au(100) alloys and the oxygen gas pressure ranging from $p_{O_2} = 5 \times 10^{-4}$ Torr to 500 Torr for the oxidation at 400 °C. It can be noted that the saturation density of oxide islands increases with the Au composition and the oxygen gas pressure, i.e., oxidation of the alloy with a larger Au composition results in a higher island density for the same oxygen pressure; the oxidation by a higher oxygen pressure leads to more dense oxide islands for the alloy with the same Au composition.

The above observations suggest that the oxide nucleation processes can be strongly influenced by the oxygen gas pressure and Au composition in the alloy. The observed

dependence of the saturation time and saturation density of oxide islands on the oxygen gas pressure as shown in Figs. 1 and 2 suggests that the oxide nucleation processes are limited by oxygen surface diffusion: The oxide nucleation results from collisions of diffusing oxygen atoms greater than a threshold. Upon formation, the critical nucleus begins to grow by capturing diffusing oxygen in its neighborhood, thus leading to a local decrease in the density of oxygen atoms. The probability of nucleating a second island within this oxygen-depleted region is correspondingly reduced because of the locally released supersaturation conditions required for island nucleation. Therefore, an active zone of oxygen capture exists around individual oxide islands, and the radius of this capture zone is proportional to the fraction of available surface area outside these zones of oxygen capture. The increase in oxygen gas pressure can significantly increase the oxygen impingement rate, thereby quickly reaching the threshold of oxygen atom density for nucleating oxide islands. Thus, the saturation time decreases while the saturated island density increases with increasing the oxygen gas pressure.

The observed increase in both the saturation time and the density of oxide islands with increasing the Au composition suggests that the oxygen surface adsorption and surface diffusion can be significantly influenced by the alloy compositions: Both the oxygen surface adsorption and surface diffusion decrease with increasing the Au composition. This is because Au does not show affinity with oxygen. Therefore, a longer time is needed to reach the threshold of oxygen atom density for nucleating oxide islands for the Cu-Au alloy with

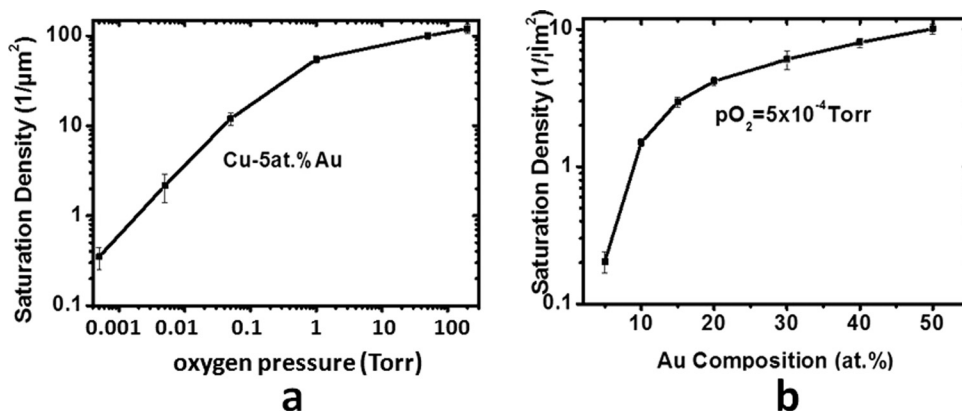


FIG. 2. (a) Dependence of the saturated density of oxide islands on the oxygen gas pressure for the oxidation of Cu-5 at. % Au(100) at 400 °C and (b) dependence of the saturated island density on the Au composition during the oxidation of Cu-Au(100) alloy at 400 °C and $p_{O_2} = 5 \times 10^{-4}$ Torr.

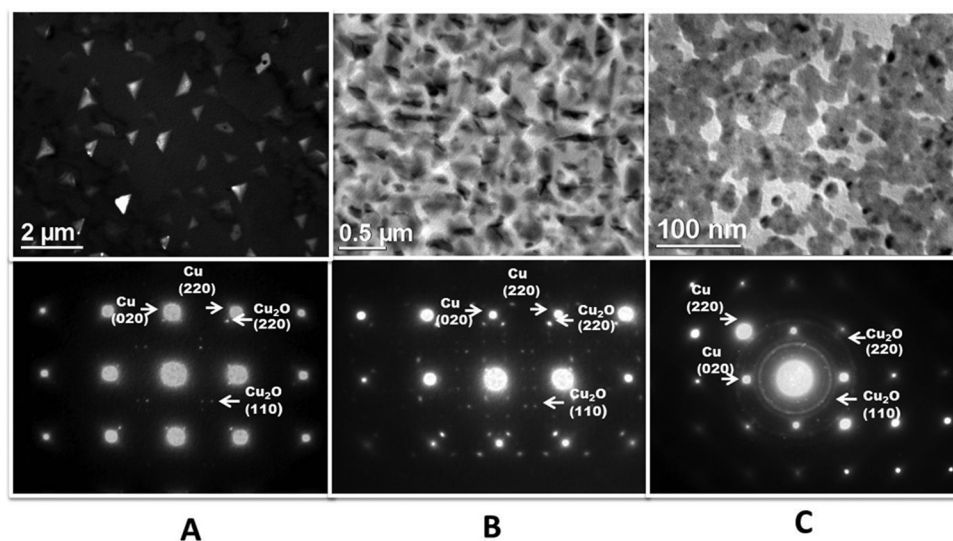


FIG. 3. (Upper panel) TEM images of Cu_2O islands formed on Cu-5 at. % Au(100) oxidized at 400°C and different oxygen pressures for 15 min, (a) $p\text{O}_2 = 5 \times 10^{-4}$ Torr, (b) $p\text{O}_2 = 0.5$ Torr, and (c) $p\text{O}_2 = 150$ Torr; (Lower panel) SAED patterns from the corresponding oxidized Cu-5 at. % Au(100) surfaces, where the additional reflections are due to double diffraction of electron beams by Cu and Cu_2O . A transition from nucleating epitaxial oxide islands to randomly oriented Cu_2O islands occurs upon increasing the oxygen pressure, as can be seen from the transition of the electron diffraction from the spot pattern to the ring pattern.

a larger Au composition, which correspondingly results in a longer saturation time for reaching the saturated island density. In addition, the reduced surface mobility of oxygen atoms for increasing the Au composition leads to a smaller capture zone of oxygen. Therefore, the attachment to an existing oxide island is less favorable than the nucleation of new nuclei, resulting in more dense oxide islands.

We then examine the effect of oxygen gas pressure on the nucleation orientations of oxide islands during the oxidation of the Cu-Au(100) alloys. Fig. 3(a) shows dark-field (using $\text{Cu}_2\text{O}(220)$ diffraction) and Figs. 3(b) and 3(c) show bright-field TEM images of a Cu-5 at. % Au(100) surface oxidized at 400°C under the different oxygen pressures for 15 min. The saturation density of oxide islands increases with the increase of oxygen partial pressure for the oxidation (note that the bright-field TEM imaging is preferred for oxide islands formed under the higher oxygen pressure for better visibility of individual islands due to the increased island density). Selected area electron diffraction (SAED) patterns of the oxidized Cu-5 at. % Au(100) surfaces confirm that the oxide islands formed from the oxidation have a Cu_2O phase. The SAED patterns show a cube-on-cube epitaxial

relationship between the oxide islands and the alloy substrates for the oxidation at lower oxygen pressures ($p\text{O}_2 < 5$ Torr), i.e., the orientation relations of $(011)\text{Cu}_2\text{O}/(011)\text{Cu-Au}$ and $[001]\text{Cu}_2\text{O}/[001]\text{Cu-Au}$ are maintained. However, for the oxidation under the oxygen pressure $p\text{O}_2 \geq 150$ Torr, SAED diffraction ring patterns are obtained, as shown in the lower panel of Fig. 3(c). The ring diffraction patterns imply that the epitaxial nucleation of Cu_2O islands is lost with the alloy substrate. The relatively uniform intensity along the diffraction rings suggests that these oxide islands are oriented randomly without preferred orientations (note that individual oxide islands are still visible for the oxidation at $p\text{O}_2 = 150$ Torr for 15 min). The appearance of additional diffraction spots or rings surrounding the Cu-Au reflections in the electron diffraction patterns shown in Fig. 3 is caused by the double diffraction of Cu_2O islands and the Cu-Au(100) substrates.

Similar behavior in the orientation transition from nucleating epitaxial Cu_2O islands to non-epitaxial oxide islands is observed for the oxidation of other alloy compositions. Fig. 4 shows TEM images and the corresponding SAED patterns of a Cu-20 at. % Au(100) film oxidized at 400°C with the different oxygen pressures for 15 min. Compared to the

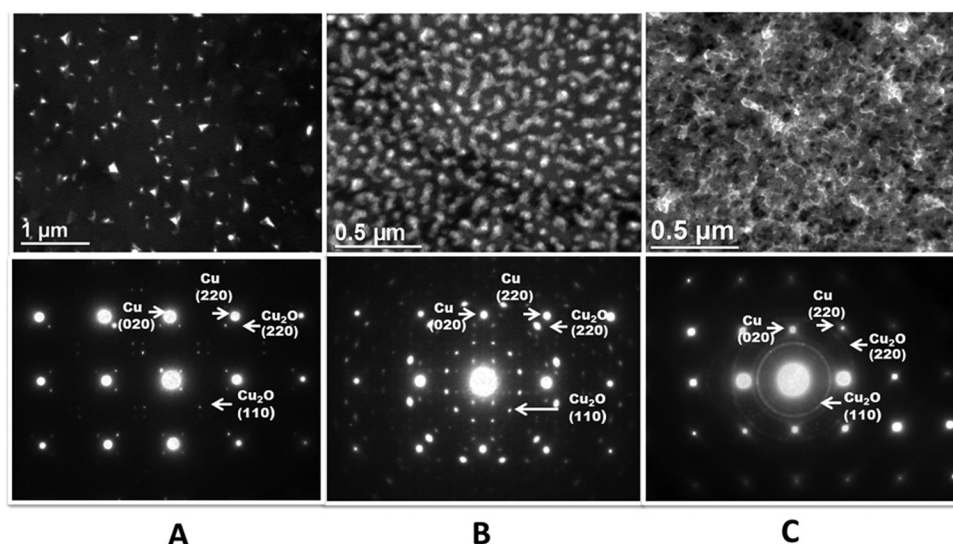


FIG. 4. (Upper panel) TEM images of Cu_2O islands formed on Cu-20 at. % Au(100) oxidized at 400°C and different oxygen pressures for 15 min, (a) $p\text{O}_2 = 5 \times 10^{-4}$ Torr, (b) $p\text{O}_2 = 0.5$ Torr, and (c) $p\text{O}_2 = 100$ Torr; (Lower panel) SAED patterns from the corresponding oxidized Cu-20 at. % Au(100) surfaces, where the additional reflections are due to double diffraction of electron beams by Cu and Cu_2O . A transition from nucleating epitaxial oxide islands to randomly oriented Cu_2O islands occurs upon increasing the oxygen pressure, as can be noted from the transition of the electron diffraction from the spot pattern to the ring pattern.

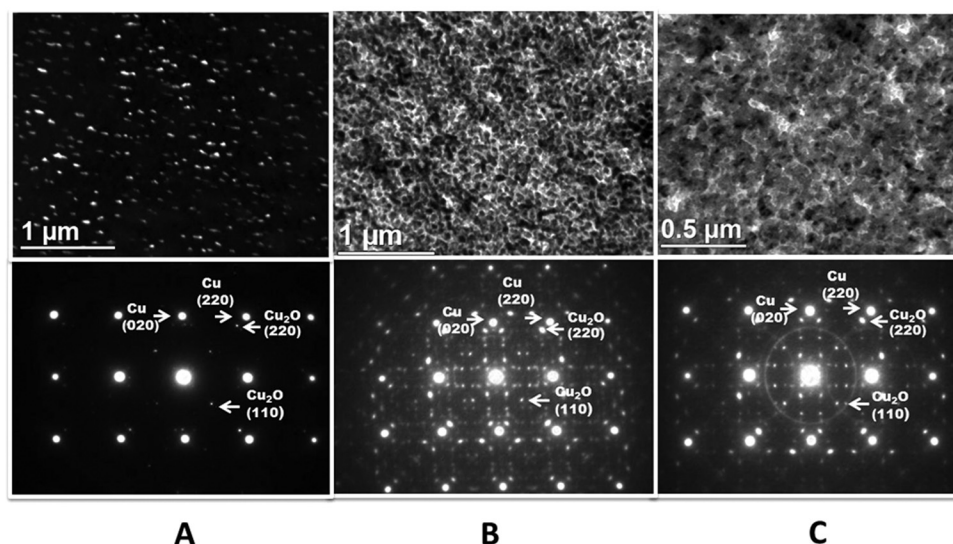


FIG. 5. (Upper panel) TEM images of Cu_2O islands formed on Cu-50 at. % Au(100) oxidized at 400°C and the different oxygen pressures for 15 min, (a) $p\text{O}_2 = 5 \times 10^{-4}$ Torr, (b) $p\text{O}_2 = 0.5$ Torr, and (c) $p\text{O}_2 = 5$ Torr; (Lower panel) SAED patterns from the corresponding oxidized Cu-50 at. % Au(100) surfaces, where the additional reflections are due to double diffraction of electron beams by Cu and Cu_2O . A transition from nucleating epitaxial oxide islands to randomly oriented Cu_2O islands occurs upon increasing the oxygen pressure, as can be noted from the transition of the electron diffraction from the spot pattern to the ring pattern.

Cu-5 at. % Au(100) sample, the island density increases but the average island size decreases for the larger Au composition. Individual oxide islands are visible for the lower oxygen gas pressures, but the oxidation at $p\text{O}_2 = 100$ Torr results in a coalesced oxide film. A significant difference from the oxidation of Cu-5 at. % Au(100) sample is that a lower oxygen gas pressure is needed in order to nucleate non-epitaxial Cu_2O islands, as shown in Fig. 4(c). This trend can be further confirmed from the oxidation of Cu-50 at. % Au(100), as shown in Fig. 5. The density of oxide islands is further increased, and the oxidation at $p\text{O}_2 = 0.5$ Torr already results in a coalesced oxide film for the larger Au composition. The transition to nucleating non-epitaxial Cu_2O islands occurs at $p\text{O}_2 = 5$ Torr, significantly lower than the Cu-Au(100) with the smaller Au compositions. A series of Cu-Au samples with different Au compositions (5 at. %, 10 at. %, 15 at. %, 20 at. %, 30 at. %, 40 at. %, and 50 at. %) has been examined from our TEM experiments, and the oxygen gas pressure required for nucleating non-epitaxial Cu_2O islands is determined from the oxidation of these different Cu-Au(100)

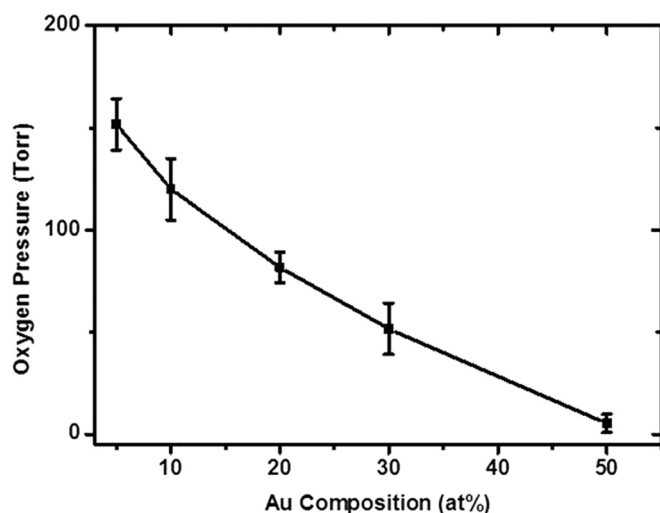


FIG. 6. Dependence of the critical oxygen gas pressure for nucleating non-epitaxial Cu_2O islands on the Au composition during the oxidation of Cu-Au(100) alloy at 400°C .

alloys at 400°C . Fig. 6 shows the determined dependence of the oxygen gas pressure on the Au composition for nucleating non-epitaxial Cu_2O islands on the Cu-Au(100) substrates. A clear trend identified from these samples is that the critical oxygen gas pressure leading to the orientation transition from nucleating epitaxial oxide islands to nucleating randomly oriented Cu_2O islands during the oxidation decreases with increasing the Au composition in the alloys.

The oxidized Cu-Au(100) samples were also examined by high-resolution TEM imaging, which provides better spatial resolution for determining the dependence of the orientations of oxide islands on the oxygen gas pressure. Fig. 7(a) shows a [001] zone-axis HRTEM image of Cu_2O nuclei on Cu-5 at. % Au(100) surface oxidized at $p\text{O}_2 = 0.005$ Torr and $T = 400^\circ\text{C}$. Two-dimensional (2D) moiré fringe pattern caused by the overlapping of Cu_2O and Cu-Au alloy lattices can be seen clearly in the HRTEM image. The size of the oxide nuclei observed is about 10 nm, as can be determined from the size of the regions with the moiré fringe contrast. The moiré fringes running parallel to {110} lattice planes of the Cu-Au(100) substrate suggest that the Cu_2O nuclei have the cube-on-cube epitaxy with the Cu-Au lattices, i.e., the equivalent planes and directions of Cu_2O islands and the Cu-Au substrate are matched. This epitaxial relationship of oxide nuclei with the Cu-Au(100) substrate is also confirmed by the Fourier transform pattern of the HRTEM image as shown in the inset, which shows the same feature as the SAED pattern, as given in Fig. 3(a). Fig. 7(b) is an HRTEM image from the oxidation of the Cu-5 at. % Au(100) sample at $p\text{O}_2 = 150$ Torr and $T = 400^\circ\text{C}$. Individual Cu_2O islands are still visible despite the increased island density, and the average size of oxide islands is about 4 nm. No moiré fringe contrast is visible in the HRTEM image, indicating that Cu_2O islands and the substrate have no epitaxial relationship, i.e., the oxide islands are oriented randomly with the Cu-Au substrate. The Fourier transform pattern of the HRTEM image is similar as the SAED pattern shown in Fig. 3(c), confirming the nature of non-epitaxial orientations of oxide islands with the Cu-Au(100) substrate. The small sizes of the epitaxial and non-epitaxial oxide islands observed in these

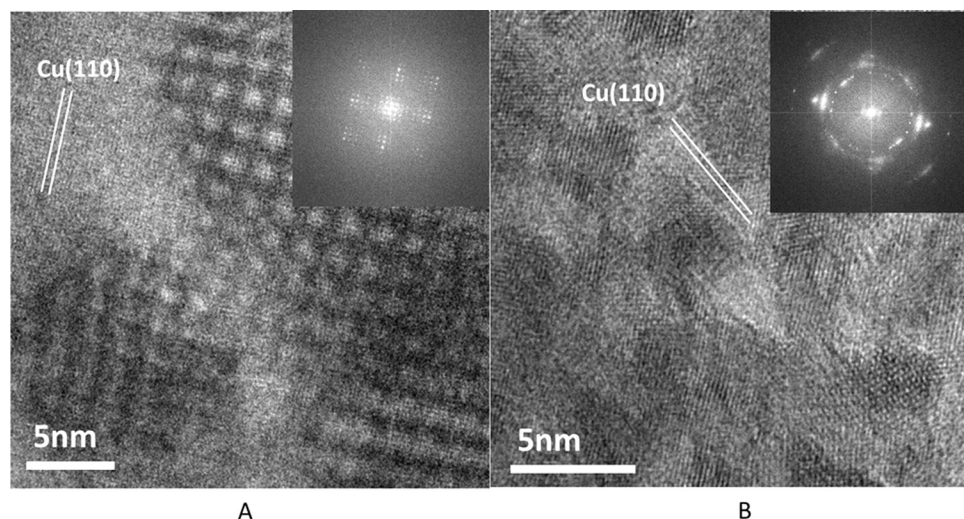


FIG. 7. HRTEM images of Cu-5 at. % Au(100) oxidized under different oxygen pressures. (a) $pO_2 = 5 \times 10^{-3}$ Torr and (b) $pO_2 = 150$ Torr. The strong 2D moiré fringe pattern in (a) implies the epitaxial nucleation of Cu_2O islands; the absence of 2D moiré fringes in (b) suggests the non-epitaxial nucleation of Cu_2O islands on the surface. The inset is the Fourier transform of the HRTEM images, which reveal the similar diffraction patterns as shown in Figure 3.

HRTEM images suggest that the orientations of the oxide islands are already set up in the very early stage of the oxide formation.

The above observations indicate that increasing the oxygen gas pressure leads to the transitions from nucleating epitaxial oxide islands to nucleating non-epitaxial oxide islands, and the oxygen pressure required for such a transition decreases with increasing the amount of Au alloyed with Cu. Nevertheless, it is crucial to confirm that the observed random orientations of oxide nuclei on the Cu-Au surfaces indeed result from the initial stage of oxide nucleation rather than from the evolution of orientations of oxide islands caused by oxide growth and coalescence. Therefore, we examined the evolution of orientations of oxide islands as a function of oxidation time. As an example, Fig. 8 shows bright-field TEM images and the corresponding SAED patterns obtained from the oxidation of Cu-20 at. % Au(100) surfaces at 400°C for 30 min with the oxygen gas pressures of $pO_2 = 0.5$ Torr, 5 Torr, and 50 Torr, respectively (note that the oxygen pressure required for forming non-epitaxial Cu_2O islands is ~ 80 Torr for this alloy composition). As shown in Figs. 8(a) and 8(b), oxide islands are still visible for $pO_2 = 0.5$ Torr and 5 Torr, and the epitaxial relationship of

the oxide islands with the Cu-Au(100) substrates is maintained despite the longer oxidation time compared to Fig. 4, where the Cu-20 at. % Au(100) sample was oxidized for only 15 min. For the oxidation at $pO_2 = 50$ Torr, oxide islands have already coalesced to form a continuous oxide film, as shown in the Fig. 8(c), and the SAED pattern shows that the oxide film is still epitaxial with the Cu-Au(100) substrate. The observations suggest that oxide islands undergo no significant change in crystallographic orientations during the oxide growth. Similar experiments were performed on Cu-Au(100) samples with other Au compositions, and it is found that the epitaxial relation of oxide islands (and the continuous oxide films after coalescence) with the Cu-Au substrate is maintained during continued oxidation if the oxygen gas pressure is below the critical oxygen pressure for nucleating non-epitaxial oxide islands. These observations indicate the orientations of oxide islands are largely determined in the stages of oxide nucleation rather than from later stages of oxide growth.

The orientation of an island may vary with the island size during thin film deposition, depending on the interfacial interaction between the island and substrate in addition to the kinetics. Such a size dependent orientation has been

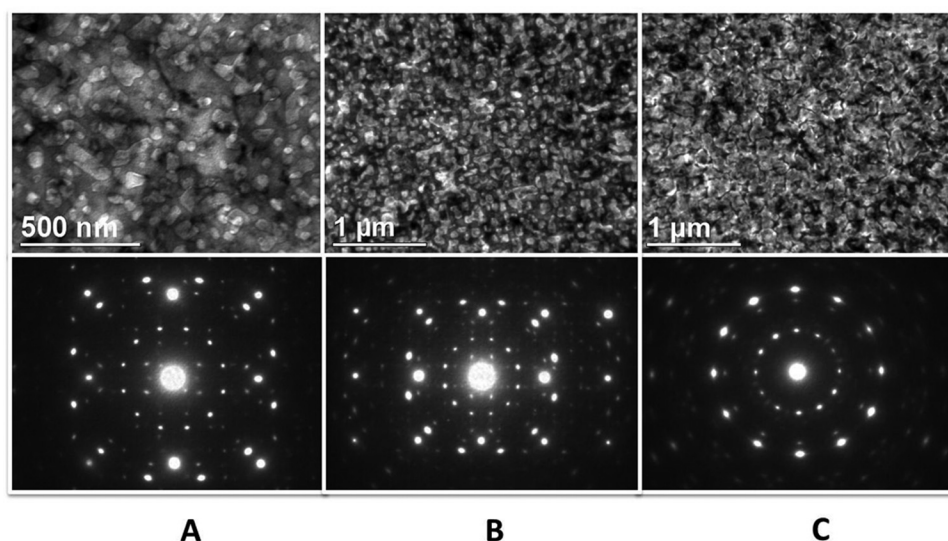


FIG. 8. Upper panel: Bright-field TEM images of Cu_2O islands formed on Cu-20 at. % Au(100) oxidized at 400°C and the different oxygen pressures for 30 min, (a) $pO_2 = 0.5$ Torr, (b) $pO_2 = 5$ Torr, and (c) $pO_2 = 50$ Torr. Lower panel: SAED patterns from the corresponding oxidized Cu-20 at. % Au(100) surfaces. The observations reveal that the cube-on-cube epitaxial orientation is still maintained during the growth and coalescence processes of the oxide islands.

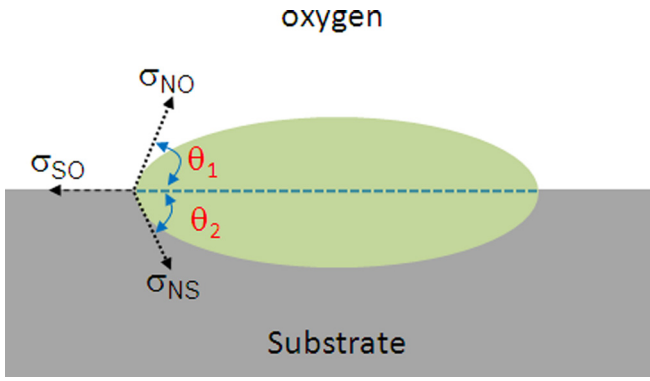


FIG. 9. Heterogeneous nucleation of a double cap-shaped oxide island on an alloy substrate, where the oxide nucleus embeds into the substrate due to the incorporation of underlying substrate atoms into the oxide phase. The contact angles for the upper and bottom caps are θ_1 and θ_2 , respectively. σ_{NO} , σ_{NS} , and σ_{SO} represent the energies of the interfaces between the nucleus and oxygen gas, nucleus and substrate, and substrate and oxygen gas, respectively.

observed in various epitaxial systems such as metal clusters (Ag, Au, Pd, and Pt) supported on MgO(100)³¹ or Si(111) substrates.^{32–34} However, such size dependent orientation is not observed for oxide islanding during the oxidation of Cu in our experiments. This is because the nucleation of an oxide island requires reaction between surface oxygen and the underlying metal substrate, this causes oxide nuclei embedding into the metal substrate, as schematically shown in Fig. 9. Therefore, the orientation of an oxide island is largely determined in the initial stages of oxide nucleation and is less likely to adjust its orientation in the later stages of growth due to the confinement by the substrate. This is consistent with our observations, as shown in Fig. 8, which demonstrates that the cube-on-cube epitaxy is maintained during the growth and coalescence of oxide islands as a function of oxidation time.

IV. DISCUSSION

The most striking observation from our experiments is the transition from nucleating epitaxial oxide islands to non-epitaxial oxide islands by increasing the oxygen gas pressure and the dependence of the critical oxygen pressure required for such an orientation transition on the Au composition in the Cu-Au alloys. To understand this behavior, we first look at the effect of Au composition on the thermodynamics of oxide nucleation on Cu-Au surface. Considering a typical three-dimensional nucleation on a plane Cu-Au surface, the free energy change ΔG that drives the oxidation reaction can be determined for the alloy oxidation reaction $2\text{Cu}_{1-x}\text{Au}_x + \frac{1}{2}\text{O}_2 \rightarrow \text{Cu}_2\text{O}$ by assuming Cu-Au as an ideal solution,

$$\Delta G = V \times \left(\Delta G^0 - 2RT \ln(1 - x_{\text{Au}}) - \frac{RT}{2} \ln(p\text{O}_2) \right), \quad (1)$$

where V is the volume of the oxide nucleus, ΔG^0 is the standard free energy change for the formation of Cu_2O which can be calculated by the equation $\Delta G^0 = -130930 + 94.5T$ (J/mole),³⁵ where R is the gas constant, T is the oxidation temperature, x_{Au} is the mole fraction of Au in the

$\text{Cu}_{1-x}\text{Au}_x$ alloy, and $p\text{O}_2$ is the oxygen partial pressure. We can obtain the dependence of the equilibrium oxygen pressure, $p\text{O}_2^e$, on the alloy composition by letting $\Delta G = 0$,

$$p\text{O}_2^e = \frac{1}{(1 - x_{\text{Au}})^4} \exp\left(\frac{2\Delta G^0}{RT}\right). \quad (2)$$

We then examine the kinetics of oxide nucleation and determine how it depends on the alloy composition and oxygen gas pressure. By assuming a double cap-shaped oxide island with the metal substrate by considering the effect of oxide island embedment into the metal substrate, as shown in Fig. 9, the interfacial contact angles, θ_1 and θ_2 , with the substrate can be related by the energy equilibrium condition $\sigma_{NO} \cos\theta_1 + \sigma_{NS} \cos\theta_2 - \sigma_{SO} = 0$, where σ_{NO} , σ_{NS} , and σ_{SO} are the interface energies, respectively, for the interfaces between the oxide nucleus and oxygen gas, nucleus and substrate, and substrate and oxygen gas. Based on the classic heterogeneous nucleation theory, the nucleation rate of oxide islands, defined as the number of stable nuclei created per area-time, can be obtained as³⁶

$$\frac{J}{B} = h'(\theta_1, \theta_2) p\text{O}_2 \ln\left(\frac{p\text{O}_2}{p\text{O}_2^e}\right) \times \exp\left(-\frac{64\pi\Omega^2\sigma_{NO}^3 h(\theta_1, \theta_2)}{3(kT)^3 \left[\ln\left(\frac{p\text{O}_2}{p\text{O}_2^e}\right)\right]^2}\right), \quad (3)$$

with $h'(\theta_1, \theta_2) = \left[(\gamma - 1) \sin\theta_1 + \frac{\sigma_{NS}}{\sigma_{NO}} \sin\theta_2 \right] [f(\theta_1)]^{-1/2}$, $h(\theta_1, \theta_2) = \frac{\gamma}{\gamma - 1} \left(\frac{\gamma - 1}{\gamma} + \frac{\sin\theta_2 \sigma_{NS}}{\gamma \sin\theta_1 \sigma_{NO}} \right) f(\theta_1)$, and $B = \frac{a_0 s N_0}{4\sqrt{2\pi m \sigma_{NO}}} \exp\left(\frac{E_{des} - E_{sd}}{kT}\right)$. $h(\theta_1, \theta_2)$ and $h'(\theta_1, \theta_2)$ are defined as the interfacial correlation functions that govern the influence of surface oxidation on the critical nucleation barrier, in which $\gamma = V_{ox}/V_m$ is called Pilling-Bedworth ratio, where V_m and V_{ox} are the molar volume of the metal and the oxide, respectively, and $\gamma = a_{\text{Cu}_2\text{O}}^3/a_{\text{Cu-Au}}^3$, where $a_{\text{Cu}_2\text{O}}$ and $a_{\text{Cu-Au}}$ are the lattice constants of Cu_2O and Cu-Au alloys, respectively. The lattice constant of an alloy depends on the alloy composition. According to Vegard's Law, the lattice constant of a $\text{Cu}_{1-x}\text{Au}_x$ solution is determined as

$$a_{\text{Cu}_{1-x}\text{Au}_x} = a_{\text{Au}} \times x_{\text{Au}} + a_{\text{Cu}} \times (1 - x_{\text{Au}}), \quad (4)$$

where a_{Cu} and a_{Au} are the lattice constants of copper and gold ($a_{\text{Cu}} = 3.615 \text{ \AA}$, $a_{\text{Au}} = 4.08 \text{ \AA}$), respectively. $f(\theta_1) = \frac{(2 + \cos\theta_1)(1 - \cos\theta_1)^2}{4}$ in Eq. (3) is the geometrical factor for a plane surface, Ω is the volume of an oxygen atom in the oxide phase, s the oxygen sticking coefficient, N_0 the density of available oxygen adsorption sites, m the molecular mass of oxygen, E_{sd} the activation energy for O surface diffusion, E_{des} the activation energy for desorption, k the Boltzmann's constant, and T the oxidation temperature.

To obtain the effect of alloy composition on the nucleation orientations of oxide islands, we introduce a parameter $n = \cos\theta_1$ for characterizing the degree of structure match at

the interface between the oxide nucleus and the alloy substrate. For a given system, the strong interaction and ideal structural match (i.e., epitaxial nucleation) lead to the complete wetting of the oxide phase with the substrate and result in the contact angles $\theta_1 + \theta_2 = 0$ and thus $n \rightarrow 1$; on the other hand, the weak interaction and poor structural match (i.e., non-epitaxial nucleation) lead to nonwetting of the oxide phase with the structure and thus result in the contact angles of $\theta_1 = 180^\circ$, $\theta_2 = 0^\circ$, and correspondingly $n \rightarrow -1$. Therefore, heterogeneous nucleation of oxide islands during the oxidation occurs in the range between $n = 1$ and $n = -1$. By substituting n and Eqs. (2) and (4) into Eq. (3), we can obtain the nucleation rate J/B as a function of the structure match parameter n for different oxygen gas pressures and alloy compositions. As an example shown in Fig. 10(a), the nucleation rate J/B is plotted via n for different p_{O_2} for the oxidation of Cu-20 at. % Au(100) alloy at 400°C . As seen in the plots, the oxidation of the Cu-Au alloy is dominated by epitaxial nucleation of oxide islands (e.g., $n = 1$) for the low oxygen pressure. With the increase in oxygen gas pressure, the non-epitaxial nucleation (e.g., $n = -1$) of oxide islands is promoted, and the difference in nucleation rates between epitaxial and non-epitaxial nucleation is dramatically reduced. Therefore, both epitaxial and non-epitaxial oxide islands are nucleated simultaneously on the alloy surface under the high oxygen pressure.

The effect of alloy composition on the nucleation orientation transition of oxide islands is illustrated in Fig. 10(b). The nucleation rate J/B is plotted via n for the several Au compositions x_{Au} for the oxidation of the Cu-Au alloys at 400°C under the same oxygen pressure ($p_{O_2} = 100\text{ Torr}$). As can be seen from the plots, the oxidation of alloy surface is

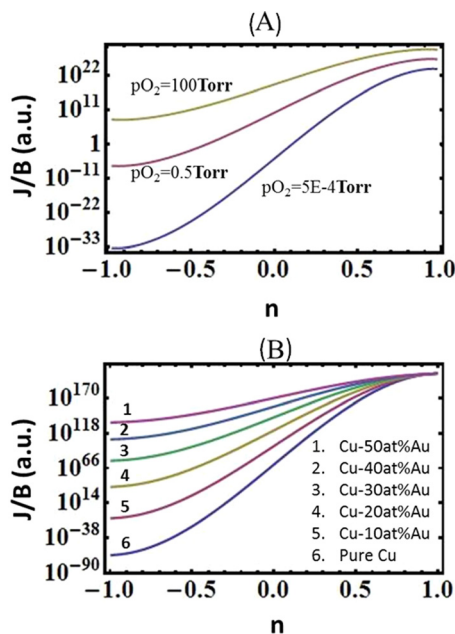


FIG. 10. (a) Plots of the relative steady-state nucleation rate J/B vs. the interaction parameter n at the different oxygen pressures p_{O_2} for oxidation of Cu-20 at. % Au(100) at 400°C ; (b) Plots of the relative steady-state nucleation rate J/B vs. the interaction parameter n for the oxidation of Cu-Au(100) with the different Au compositions at $p_{O_2} = 100\text{ Torr}$ and $T = 400^\circ\text{C}$.

dominated by epitaxial nucleation of oxide islands for Cu-Au alloy with Au composition $x_{\text{Au}} < 20\%$ while non-epitaxial nucleation of oxides is highly promoted for Cu-Au alloy with Au composition $x_{\text{Au}} > 20\%$. Therefore, both epitaxial and non-epitaxial oxide islands are nucleated simultaneously on the Cu-Au alloy surface with a higher Au composition while the oxygen pressure remains the same for the different alloys. It can be seen that the higher Au composition is in the Cu-Au alloy, the lower the critical oxygen pressure becomes for nucleating non-epitaxial oxide islands. Although quantitative comparison between the nucleation rates of experimental data and the model by Eq. (3) cannot be made due to practical limitations of the classic heterogeneous nucleation theory including the lack of the accurate values of surface and interface energies and the surface diffusion rates as a function of oxygen pressure, which makes the theory difficult to quantify, the real data of the experimental oxygen gas pressures and Cu-Au alloy compositions are used in the model to predict the effect of oxygen gas pressure and alloy compositions on the nucleation orientations of oxide islands during the oxidation. The outcome of the model as shown in Fig. 10 provides reasonable match with the ranges of the oxygen pressure and alloy compositions at which the orientation transitions of oxide islands from epitaxial to non-epitaxial nucleation are experimentally observed, where the oxygen pressure leading to nucleation of randomly oriented oxide islands decreases from 150 Torr to 5 Torr when the Au composition increases from 5 at. % to 50 at. %.

As the above discussion illustrates, the epitaxial nucleation of oxide islands cannot be maintained throughout the whole range of oxygen pressure, and increasing Au composition in the Cu-Au alloy results in a decrease in the critical oxygen pressure leading to the orientation transition to nucleating non-epitaxial oxide islands. The physical understanding of such an effect of the alloy composition on the orientations of oxide nuclei can be understood as follows. The rate of forming critical oxide nuclei is determined by two competing factors, i.e., nucleation barrier and the effective atom collision rate factors. At the low oxygen pressure, the nucleation barrier is high and the nucleation rate is dominated by the exponential term in Eq. (3). Therefore, oxide islands with a lower nucleation barrier show a faster nucleation rate. Thus, the nucleation of oxide islands with the strong interaction and good structural match ($n = 1$) between oxide nuclei and substrate is kinetically favorable. Conversely, at high oxygen pressures, the nucleation barrier is reduced and the issue of effective collisions, described by the collisional pre-factor of Eq. (4), becomes more important. The nucleation of oxide islands with weak interaction and poor structural match ($n \rightarrow 0$, and -1) with the substrate is enhanced. The critical oxygen gas pressure leading to such an orientation transition of oxide nuclei can be modified by the alloy composition via its effect on the nucleation barrier. By adding more Au into the Cu-Au alloy, the lattice mismatch between the oxide and the alloy substrate is reduced, thereby lowering the nucleation barrier for their better structure match. Therefore, increasing Au mole fraction in the alloy leads to a decrease in the nucleation barrier, as measured in our previous work.³⁷ The reduced nucleation barrier

correspondingly results in a lower critical oxygen gas pressure for nucleating non-epitaxial oxide islands. It is noted that the equilibrium oxygen pressure, pO_2^e , given in Eq. (2), for the formation of Cu_2O oxide on the Cu-Au alloy surface is also changed by the alloy composition but has a relatively minor effect on the nucleation rate of oxide islands, especially under the very high supersaturation, $\frac{pO_2}{pO_2^e}$, of the oxygen pressure.

V. CONCLUSION

In conclusion, an orientation transition from nucleating epitaxial to non-epitaxial Cu_2O islands is observed by increasing the oxygen gas pressure during the initial stages of oxidation of Cu-Au(100). The effect of Au composition on the critical oxygen gas pressure required for such an orientation transition of oxide nuclei is monitored by *in situ* environmental TEM. It is found that the critical oxygen pressure for this transition decreases with the increase of Au composition in the Cu-Au alloys. Such a dependence of the critical oxygen gas pressure on the alloy composition is ascribed to its effect on the oxide nucleation barrier that alters the relative importance of two competing factors, i.e., the oxide-alloy structure match and the effective collision of atoms, in determining the oxide nucleation rate. This result is expected to provide better perception into bridging the pressure gap in the still-limited understanding of the initial-stage oxidation of alloys as well as designing alloys for controlling the orientations of oxide film coating under ambient conditions.

ACKNOWLEDGMENTS

Research was supported by the U.S. Department of Energy, Office of Basic Energy Sciences, Division of Materials Sciences and Engineering under Award No. DE-FG02-09ER46600.

¹J. Li, J. W. Mayer, and E. G. Colgan, *J. Appl. Phys.* **70**, 2820 (1991).

²W. A. Lanford, P. J. Ding, W. Wang, S. Hymes, and S. P. Murarka, *Mater. Chem. Phys.* **1995**, 192 (1995).

³S. K. Lahiri, N. K. Waalib Singh, K. W. Heng, L. Ang, and L. C. Goh, *Microelectron. J.* **29**, 335 (1998).

⁴H. Over, Y. D. Kim, A. P. Seitsonen, S. Wendt, E. Lundgren, M. Schmid, P. Varga, A. Morgante, and G. Ertl, *Science* **287**, 1474 (2000).

⁵R. Westerström, J. Gustafson, A. Resta, A. Mikkelsen, J. N. Andersen, E. Lundgren, N. Seriani, F. Mittendorfer, M. Schmid, J. Klikovits, P. Varga, M. D. Ackermann, J. W. M. Frenken, N. Kasper, and A. Stierle, *Phys. Rev. B* **76**, 155410 (2007).

⁶F. Besenbacher and J. K. Nørskov, *Prog. Surf. Sci.* **44**, 5 (1993).

⁷N. Birks, G. H. Meier, and F. S. Pettit, *Introduction to the High Temperature Oxidation of Metals* (Cambridge University Press, Cambridge, 2006).

⁸P. L. Gai and E. D. Boyes, *Microsc. Res. Tech.* **72**, 153 (2009).

⁹R. Sharma, *Microsc. Res. Tech.* **72**, 144 (2009).

¹⁰J. C. Yang, M. Yeadon, B. Kolasa, and J. M. Gibson, *Scr. Mater.* **38**, 1237 (1998).

¹¹J. C. Yang, B. Kolasa, J. M. Gibson, and M. Yeadon, *Appl. Phys. Lett.* **73**, 2841 (1998).

¹²J. C. Yang, M. D. Bharadwaj, G. W. Zhou, and L. Tropic, *Microsc. Microanal.* **7**, 486 (2001).

¹³J. C. Yang, D. Evan, and L. Tropic, *Appl. Phys. Lett.* **81**, 241 (2002).

¹⁴G. W. Zhou and J. C. Yang, *Surf. Sci.* **531**, 359 (2003); *Phys. Rev. Lett.* **89**, 106101 (2002); *J. Mater. Res.* **20**, 1684 (2005).

¹⁵N. Cabrera and N. F. Mott, *Rep. Prog. Phys.* **12**, 163 (1949).

¹⁶C. Wagner, *Z. Phys. Chem. B* **21**, 25 (1933).

¹⁷G. W. Zhou, L. Wang, R. C. Birtcher, P. M. Baldo, J. E. Pearson, J. C. Yang, and J. A. Eastman, *Phys. Rev. Lett.* **96**, 226108 (2006).

¹⁸J. Gustafson, A. Mikkelsen, M. Borg, E. Lundgren, L. Köhler, G. Kresse, M. Schmid, P. Varga, J. Yuhara, X. Torrelles, C. Quirós, and J. N. Andersen, *Phys. Rev. Lett.* **92**, 126102 (2004).

¹⁹E. Lundgren, J. Gustafson, A. Mikkelsen, J. N. Andersen, A. Stierle, H. Dosch, M. Todorova, J. Rogal, K. Reuter, and M. Scheffler, *Phys. Rev. Lett.* **92**, 046101 (2004).

²⁰W. X. Li, L. Osterlund, E. K. Vestergaard, R. T. Vang, J. Mathiesen, T. M. Pedersen, E. Lagsgaard, B. Hammer, and F. Besenbacher, *Phys. Rev. Lett.* **93**, 146104 (2004).

²¹J. A. Eastman, P. H. Fuoss, L. E. Rehn, P. M. Baldo, G. W. Zhou, D. D. Fong, and L. J. Thompson, *Appl. Phys. Lett.* **87**, 051914 (2005).

²²C. Stampfl, A. Soon, S. Piccinin, H. Q. Shi, and H. Zhang, *J. Phys.: Condens. Matter* **20**, 184021 (2008).

²³Y. B. He, A. Stierle, W. X. Li, A. Farkas, N. Kasper, and H. Over, *J. Phys. Chem. C* **112**, 11946 (2008).

²⁴K. Lahtonen, M. Hirsimäki, M. Lampimäki, and M. Valden, *J. Chem. Phys.* **129**, 124703 (2008).

²⁵S. Ferrer, M. D. Ackermann, and E. Lundgren, *MRS Bull.* **32**, 1010 (2007).

²⁶R. Westerström, C. J. Weststrate, J. Gustafson, A. Mikkelsen, J. Schnadt, J. N. Andersen, E. Lundgren, N. Seriani, F. Mittendorfer, G. Kresse, and A. Stierle, *Phys. Rev. B* **80**, 125431 (2009).

²⁷A. Vlad, A. Stierle, M. Marsman, G. Kresse, I. Costina, H. Dosch, M. Schmid, and P. Varga, *Phys. Rev. B* **81**, 115402 (2010).

²⁸L. L. Luo, Y. H. Kang, Z. Y. Liu, J. C. Yang, and G. W. Zhou, *Phys. Rev. B* **83**, 155418 (2011).

²⁹G. W. Zhou and J. C. Yang, *Phys. Rev. Lett.* **93**, 226101 (2004).

³⁰G. W. Zhou, W. Y. Dai, and J. C. Yang, *Phys. Rev. B* **77**, 245427 (2008).

³¹R. Ferrando, G. Rossi, A. C. Levi, Z. Kuntová, F. Nita, A. Jelea, C. Mottet, G. Barcaro, A. Fortunelli, and J. Goniakowski, *J. Chem. Phys.* **130**, 174702 (2009).

³²B. Q. Li and J. M. Zuo, *Surf. Sci.* **520**, 7 (2002).

³³B. Q. Li and J. M. Zuo, *J. Appl. Phys.* **94**, 743 (2003).

³⁴J. M. Zuo and B. Q. Li, *Phys. Rev. Lett.* **88**, 255502 (2002).

³⁵D. R. Gaskell, *Introduction to Metallurgical Thermodynamics* (Scripta, Washington, D.C., 1973).

³⁶G. W. Zhou, *Appl. Phys. Lett.* **94**, 201905 (2009); *Phys. Rev. B* **81**, 195440 (2010).

³⁷G. W. Zhou, J. A. Eastman, R. C. Birtcher, P. M. Baldo, J. E. Pearson, L. J. Thompson, L. Wang, and J. C. Yang, *J. Appl. Phys.* **101**, 033521 (2007).